



## DOAS FOR FLUE GAS MONITORING—I. TEMPERATURE EFFECTS IN THE U.V./VISIBLE ABSORPTION SPECTRA OF NO, NO<sub>2</sub>, SO<sub>2</sub> AND NH<sub>3</sub>

JOHAN MELLQVIST<sup>a,b</sup> and ARNE ROSÉN<sup>a</sup>

<sup>a</sup>Department of Physics, Chalmers University of Technology and Göteborg University, S-412 96 Göteborg and <sup>b</sup>The Swedish Environmental Research Institute (IVL), P.O. Box 47086, S-402 58 Göteborg, Sweden

(Received 11 December 1995)

**Abstract**—The temperature dependence of the absolute and the differential absorption cross-sections for NO, SO<sub>2</sub>, NO<sub>2</sub> and NH<sub>3</sub> were studied by recordings of spectra in a heat-pipe cell and by simulations of theoretical spectra for NO. A review and comparison of the present results with other relevant works were also made. The experimental results showed that the differential absorption features for some of the studied species change dramatically with temperature. For SO<sub>2</sub> and NO<sub>2</sub> the quantitative change in differential structure was very large with a relative change in magnitude of 70% between 300 and 700 K. For the two other species studied, NO and NH<sub>3</sub>, the change in magnitude of the differential structure was only 15–20%, over the same temperature range. Simulations for NO showed that the temperature effect was strongly dependent on the spectral resolution of the instrument and that it became smaller at lower resolution. The qualitative change in the spectral features was a continuous lowering of absorbance peaks and an increase in valleys which made the band integral of the absorbance quite insensitive to the temperature. Hot bands also appeared for SO<sub>2</sub> and NH<sub>3</sub> around 220 nm. The temperature affected the spectral features more in a quantitative than in a qualitative manner. Copyright © 1996 Elsevier Science Ltd

### 1. INTRODUCTION

Differential Absorption Spectroscopy in the u.v./visible has been utilized for more than half a century in Dobson spectrometers<sup>1</sup> which are used to monitor total columns of atmospheric ozone and in Brewer-photometers<sup>2</sup> which are used to monitor total columns of NO<sub>2</sub>, SO<sub>2</sub> and O<sub>3</sub>. It was Platt et al<sup>3</sup> who first started to utilize differential absorption for tropospheric gas composition measurements by introducing DOAS (Differential Optical Absorption Spectroscopy). The technique is based on the recording of differential absorption, i.e., the difference between local maxima and minima in the absorption spectrum of the probed gas species. In the tropospheric application, light from a broadband xenon high-pressure lamp is transmitted through the atmosphere for distances up to several kilometers. The light is received and analyzed using a fast scanning device to eliminate the influence of air turbulence. The most straightforward atmospheric molecules to detect with DOAS are probably NO<sub>2</sub>, O<sub>3</sub> and SO<sub>2</sub>, and these species are also routinely monitored in many cities around the world.<sup>4,5</sup> Other species that have been monitored, but which require more advanced instrumentation are: CH<sub>2</sub>O, CS<sub>2</sub>, Hg, HNO<sub>2</sub>, NH<sub>3</sub>, NO, NO<sub>3</sub> and OH.<sup>6–9</sup> It is also feasible to measure light aromatic hydrocarbons such as benzene, toluene and xylenes.<sup>10,11</sup> The absorption features of the latter molecules are however very similar and interfere severely. By using scattered sunlight it has also been possible to perform total column measurements on the atmosphere for species such as NO<sub>2</sub> and O<sub>3</sub> but also for OClO, BrO and NO<sub>3</sub>.<sup>12–16</sup> It has furthermore been possible to obtain information on aerosol density and size distribution in the stratosphere.<sup>17</sup> An interesting application of the DOAS technique is to use it for *in-situ* detection, across the stack, of flue gases, since many of the main pollutants from fossil fuel combustion can be detected with the technique. The feasibility of using the technique *in-situ* is attractive in order to minimize response times and in order to detect polar and reactive gases which can be very difficult to measure

extractively. The direct application of the DOAS technique is however not possible, since the flue gases can have high temperatures (20–1000°C) which may affect the differential absorption cross-sections significantly. In addition, the optical pathlengths are determined by the dimensions of the flue gas channels, which can lead to such large optical depths that the absorption of the gases will deviate from the Beer–Lambert law and become nonlinear.<sup>18–20</sup>

The increased use of u.v./visible absorption techniques for industrial monitoring applications, and the fact that most of the development is being performed on a commercial basis, therefore makes it important to focus on these problems. To our knowledge, no detailed investigations have been performed for the u.v./visible range. The nonlinearity effects have been covered in a separate publication,<sup>21</sup> Paper II in this series, while in this paper the temperature effects were studied in the u.v./visible by recordings of experimental spectra, spectral simulations and a review of the literature. A rather detailed description of the DOAS technique will also be given. In an additional paper,<sup>22</sup> Paper III, results from a field experiment will be demonstrated where DOAS measurements were performed in flue gases and then compensated for temperature and nonlinearity effects by a methodology developed from this paper and Paper II.<sup>21</sup>

## 2. EXPERIMENTAL SYSTEM AND PROCEDURE

### 2.1. Optical setup

The DOAS instrument that was used in this study is of the same design as that introduced by Platt and Perner.<sup>4</sup> A schematic of the instrument is shown in Fig. 1. ultraviolet/visible light from a 150 W xenon arc lamp (Hamamatsu L2273) was transmitted along a measurement path by Newtonian telescopes and then focused on to the entrance slit (100  $\mu\text{m}$ ) of a Thermo Jarrel–Ash spectrometer (275 mm, f/3.8 Czerny–Turner). The spectrometer was equipped with a rotating slotted disc device, replacing the exit slit, which consisted of a round disc (radius 10 cm), with 20 radially etched slits with a width of 100  $\mu\text{m}$ . An EMI 9750 QB photomultiplier tube was used to detect the transmitted light by taking 1024 samples during one scan, i.e., during the passage of each slit in front of the focal plane of the spectrometer. The signal was amplified and sent to a PC with a custom-made MCA (multichannel analyzer) plug-in card with a 12-bit A/D converter, dividing each scan into

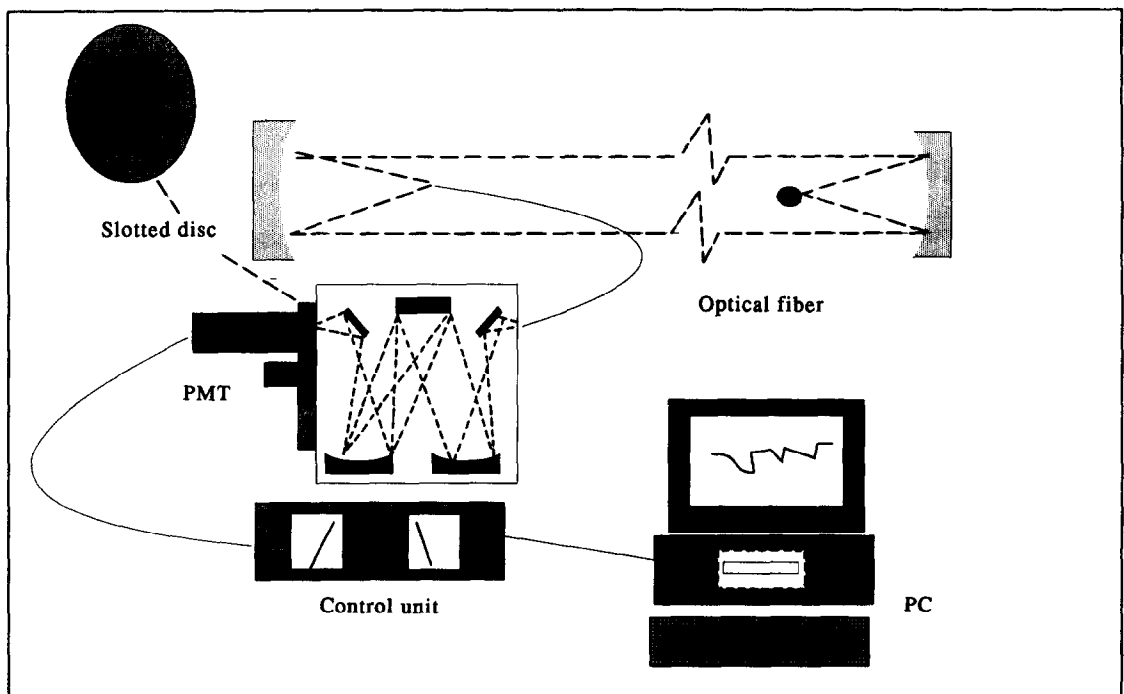


Fig. 1. A schematic drawing of the DOAS instrumentation.

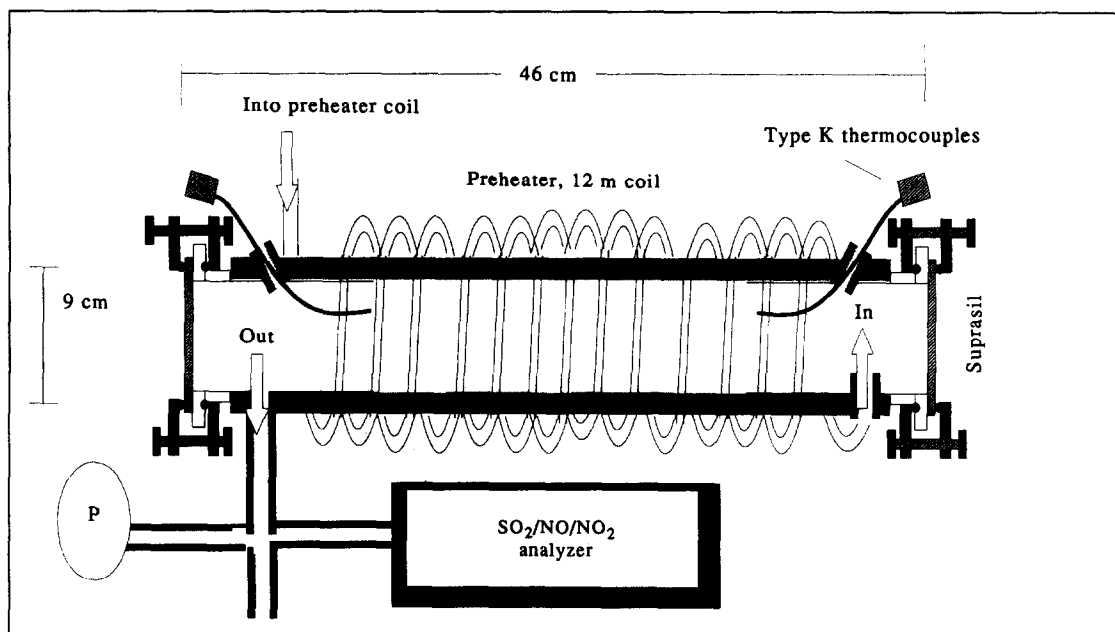


Fig. 2. A schematic drawing of the Pyrex™ measurement cell.

1024 channels. After sampling of  $10^3$ – $2 \cdot 10^4$  scans, the data were transferred to the computer for signal processing. The measurement time for each scan of the spectrum was 16 msec.

In this study, a mechanically grooved grating, blazed at 260 nm, was used with a grating constant of 2400 grooves/mm, yielding a spectral coverage of approximately 34 nm. Due to the use of the slotted disc setup the spectral resolution was best in the middle of the spectrum, and was degraded by approximately 30% at both ends, due to slightly tilted slits in these parts of the scan. This resulted in spectral resolutions (FWHM) of 0.23 nm for  $\text{NO}_2$  around 430 nm and  $\text{SO}_2$  around 300 nm. The resolution was 0.3 nm for NO and 0.24 nm for  $\text{SO}_2$  and  $\text{NH}_3$  around 226 and 215 nm, respectively. The spectral resolution was entirely caused by the finite size of the entrance and exit slits.

## 2.2. Experimental equipment for calibration of gases

Preliminary measurements of the differential absorption cross-sections of  $\text{SO}_2$ ,  $\text{NO}_2$  and NO in the temperature range 20–400°C were reported in a previous paper.<sup>18</sup> The measurements were performed in a stainless steel cell. A major uncertainty in that study was whether any potential adsorption of the various gases occurred during these measurements and whether this would result in heterogeneous reactions. To improve the accuracy and reliability of the measurements the experimental setup was redesigned, with the material of the original measurement cell being replaced by Pyrex™, since this material is considered to be more inert to potential adsorption. The cell, see Fig. 2, was cylindrical with a length of 0.46 m and a diameter of 9 cm (i.d.) yielding a cell volume of approximately 31. The gas flow through the cell was maintained at 7 l/min giving a residence time in the cell of approximately 25 sec. The u.v./visible light was transmitted through two silica windows (Suprasil™), which were attached to the cell by graphite seals. The measurement cell was placed in a heat-pipe oven and could be maintained at temperatures in the range of 20–500°C. The temperature was measured at two places inside the cell using type-K thermocouples, with a measurement precision of 1°C. The gas was preheated in a 12-m-long  $\frac{1}{4}$ " wide Pyrex™ tube before it entered the measurement cell. In the previous measurements,<sup>18</sup> the pressure in the cell was measured using a differential pressure gauge together with a mercury barometer. The contribution of the differential pressure to the total pressure in the cell was very small, however. In this study the influence of differential pressure was therefore neglected and the pressure was assumed to be atmospheric. In order to investigate whether any permanent chemical reactions occurred in the

measurement cell the gases were, in some cases, analyzed at the outlet of the measurement cell by conventional monitors. A fluorescence instrument (Monitor labs 8850) was used for SO<sub>2</sub> and a combined i.r. and u.v. absorption instrument (BINOS) for NO<sub>2</sub> and NO.

### 2.3. Measurement procedure

Recordings of the differential absorption cross-sections of NO, NO<sub>2</sub>, SO<sub>2</sub> and NH<sub>3</sub> were carried out with the experimental equipment described above. Each gas was continuously flowed through the measurement cell. Recordings of spectra were then made at nine temperatures between 20 and 400°C at constant gas volume-mixing-ratios. The absolute values of the differential absorption cross-sections were obtained by calculating the true number density in the measurement cell using the ideal gas law. The gases used were supplied by AGA specialgas AB in Sweden at specific volume concentrations. They were all diluted in nitrogen with a precision of 2–5% v/v and were used without further purification. For the gas species used the mixing ratios were 170 ppm ± 5% for NO<sub>2</sub>, 97.5 ppm ± 5% for NO, 196.5 ppm ± 5% for SO<sub>2</sub> and 44.6 ppm ± 3% for NH<sub>3</sub>. In the NO<sub>2</sub> gas, approximately 24 ppm NO were also present. The continuous flow of the measurement gases suppressed wall effects and other molecular losses (absorption/dissociation). To avoid photodissociation of the absorbing gases, optical filters were used for SO<sub>2</sub> and NO<sub>2</sub> with cut-off wavelengths at 240 and 410 nm, respectively. For SO<sub>2</sub> and NH<sub>3</sub> between 210 and 230 nm and NO<sub>2</sub> around 360 nm the measurements were performed below the threshold for photodissociation. Reaction rate experiments (stop flow) were therefore performed to ensure that the flow rate was sufficient to suppress the effects of photodissociation. This was carried out by flowing the species studied through the measurement cell which was maintained at 700 K and illuminated by the xenon-light source, as shown in Fig. 2. The gas flow was then stopped and the time decay of the species studied was monitored by the DOAS.

### 2.4. Retrieval algorithms

In the DOAS application, light is transmitted through the atmosphere, and the path-averaged concentration of target species in the atmosphere is obtained from the detected light intensity. The transmitted light can be described by the Beer–Lambert law:

$$I_d(\lambda, T, p, \Delta\lambda) = I_L(\lambda) \cdot F(\lambda) \cdot \exp \left[ - \sum_i \sigma_i(\lambda, T, p, \Delta\lambda) \cdot c_i \cdot x - \alpha(\lambda) \cdot x \right] \quad (1)$$

where

$I_d$  = detected light intensity,

$F(\lambda)$  = wavelength dependence of instrument

$\sigma_i$  = absorption cross-section [cm<sup>2</sup>/molecule]

$\alpha$  = attenuation coefficient from elastic scattering and aerosol absorption

$I_L$  = light source intensity

$x$  = optical measurement path

$c_i$  = path-averaged concentration

$\Delta\lambda$  = band-pass of instrument

$i$  = index for species studied.

The product of pathlength and concentration ( $c \cdot x$ ) is referred to as total column and the optical depth, OD, as  $(\sigma \cdot c \cdot x)$ . In order to obtain the total columns of the target species along the measurement path, it is necessary to derive a background spectrum, which corresponds to zero absorption of the target species. In contrary to laboratory analyses where a background spectrum can be recorded by emptying the measurement cell, there is no simple way to obtain such a spectrum in atmospheric measurements. The background, as well as the molecular absorption has instead to be *derived from a single spectrum*. It is difficult to derive a background spectrum in the u.v./visible region due to substantial and variable atmospheric scattering. Many species also exhibit broad-band absorption structures, especially with a spectrograph with a limited resolution, and these interfere with each other. These difficulties require the use of differential spectroscopy. In the

retrieval algorithms of the DOAS technique a discrimination between broad,  $I'_0$ , and narrow features,  $dI$ , is made in the intensity spectra according to:

$$I_d = I'_0(\lambda) \cdot dI(\lambda) \quad (2)$$

The broad features can be attributed to the wavelength dependence of the instrument, of the light source and of the elastic scattering processes. They are also caused by the broad features of the molecular absorption, which we denote by a pseudo-absorption cross-section:  $\sigma_0$ . The broad features are derived by fitting a low-order polynomial,  $I_p$ , (1st–6th order) to the recorded spectrum, and this polynomial is assumed to correspond to the term on the right hand side in Eq. (3) below. The polynomial fitting will give the same results as a low-pass filtering of the recorded intensity spectrum, where the cut-off frequency is defined by the order of the polynomial.

$$I'_0(\lambda) = I_p(\lambda) = I_L(\lambda) \cdot F(\lambda) \cdot \exp \left[ - \sum_i \sigma_{0,i}(\lambda, T, p) \cdot c_i \cdot x - \alpha(\lambda) \cdot x \right] \quad (3)$$

The narrow features in the detected intensity spectrum can be attributed solely to the narrow absorption features of the molecule, denoted by  $d\sigma$ . These features will contain information on the total column of target molecules in the spectrum. By using Eqs. (1), (2) and (3) one can derive the differential absorbance,  $dA$ , which is utilized in the DOAS technique:

$$\ln \left( \frac{I_d(\lambda)}{I_p(\lambda)} \right) = \left[ - \sum_i \sigma_{i,d}(\lambda) - \sigma_{0,d}(\lambda) \right] \cdot c \cdot x = \left[ \sum_i d\sigma_i(\lambda) \right] \cdot c \cdot x = dA \quad (4)$$

where  $d\sigma$  corresponds to the differential absorption cross-section.

The principle of differential absorption is visualized in Fig. 3. A recorded spectrum of  $\text{SO}_2$  is displayed corresponding to a partial pressure of  $2 \cdot 10^{-4}$  atm at a pathlength of 0.46 m. In addition, a fitted 5th order polynomial spectrum is shown corresponding to  $I'_0$ . By applying Eq. (4) on the spectrum to the left in Fig. 3, the spectrum to the right will be obtained corresponding to the differential absorbance.

Equation (3) is fundamental in the retrieval routines of the DOAS technique. The broad-band absorption cross-section,  $\sigma_0$ , and consequently also the differential absorption cross-section,  $d\sigma = \sigma - \sigma_0$ , are obtained and defined in this equation by the polynomial fitting. In a strict sense, Eq. (3) can only be applied at small optical depths however. In order to define the broad and differential absorption cross-section in a stringent manner, the polynomial fitting or low-pass filtering should be performed in the absorbance domain and not in the intensity domain which is done in Eq. (3). This is due to the fact that the frequency distribution in the intensity domain is dependent on the optical depth, i.e., the larger the optical depth the broader are the spectral features (*frequency here corresponds to the variation of the spectral features and not to energy or wavelength*). The frequency distribution of the spectral features will thus be dependent on the total columns at

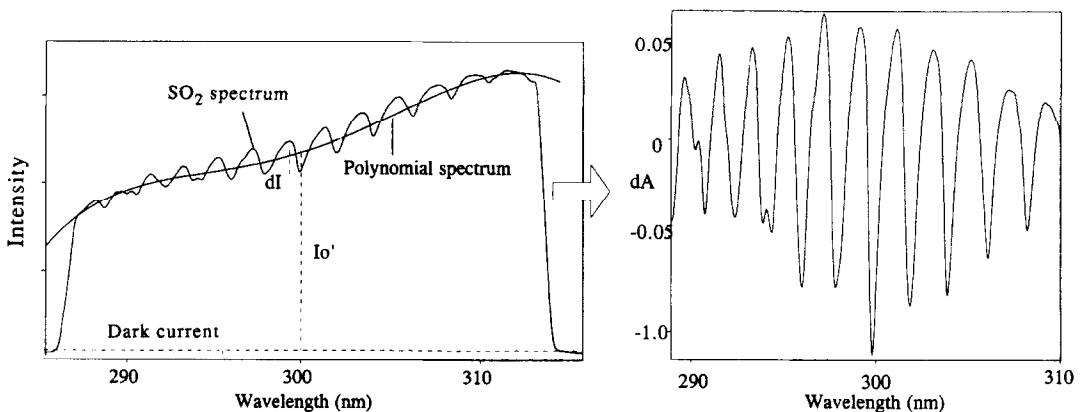


Fig. 3. A DOAS intensity spectrum (arbitrary units) recorded in a 0.46 m long cell, containing  $2 \cdot 10^{-4}$  atm of  $\text{SO}_2$  and a fitted 5th order polynomial is shown to the left. To the right the corresponding differential absorbance spectrum is shown.

large ODs and this may in turn affect the appearance of the broad-band and differential absorption cross-sections.

For low ODs, which are most common in the atmospheric application, Eq. (3) performs well, since the exponential in the Beer–Lambert law is linear and the polynomial fitting or low-pass filtering in the intensity domain is then equal to the low-pass filtering in the cross-section domain. Also for larger ODs it is usually possible to use Eq. (3) since the polynomial is of such low order so that even if the narrow absorption features of the molecule have broadened, they are still much narrower than the polynomial. One should be aware of the problem above, however, and be cautious when utilizing polynomials of high orders at large optical depths.

One relatively simple way to solve the problem above would be to perform the logarithmic transformation prior to the polynomial fitting so that all fittings are performed in the cross-section domain. Another way would be to use spline fitting, in which cubic or linear splines are fitted through certain fixed wavelength points in the intensity spectrum. The differential absorption cross-sections will then be defined as the difference between the true absorption cross-sections and the spline. This is similar to the approach which is used in the DIAL technique,<sup>23</sup> where the difference in absorption between two wavelengths close to each other is used to obtain concentration information. In this study we have in most cases used the normal DOAS retrieval algorithms, but for NO, NO<sub>2</sub> and NH<sub>3</sub> spline fitting have in some cases also been used.

By fitting recorded laboratory spectra to atmospheric differential absorbance spectra, it is possible to retrieve the *path-averaged* concentration of various molecules along the optical measurement path. In this study, the fitting procedure was performed by multiple linear regression in accordance with Bevington.<sup>24</sup> In this procedure, the laboratory spectra were fitted linearly to the experimental spectra, by calculation of a scaling factor and a baseline, yielding the smallest variance between the two spectra. The correlation coefficient and standard deviation between the fitted and experimental spectrum were also calculated in the fitting procedure and used as good indicators of the quality of the measurements. Before normalizing the recorded intensity spectrum according to Eq. (4), the background, which is caused by thermal noise in the detector and amplifier, was subtracted from the intensity spectrum. A typical background caused by dark current in the PM tube was displayed in Fig. 3. In many applications the intensity spectrum is also first normalized with a lamp spectrum, or if possible, a reference spectrum recorded with the actual optical setup but in clean air. This will eliminate narrow spectral structures caused by the lamp and the spectrometer, which may otherwise disturb the spectral evaluation. In some applications the polynomial may be substituted by a spline fitted to the background. The full retrieval algorithms of the recorded DOAS spectra in this study were consistent with the procedures of Platt and Perner<sup>4</sup> and can be summarized with the following operations which were performed on the recorded intensity spectra: (I) background subtraction, (II) normalization with lamp- or a clean air reference, (III) normalization with a fitted polynomial (1st–5th order), (IV) logarithmic transformation, (V) spectral fitting to calibration spectra.

### 3. SIMULATIONS OF DOAS SPECTRA

Absorption spectra of NO were simulated, corresponding to the spectra that were recorded by the DOAS instrument in this study. The spectra were simulated at various temperatures and column densities in order to investigate how well the spectra obeyed the Beer–Lambert law and how the spectral features were affected by the temperature. The method of spectral calculation will be presented in this section, while the results will be presented in Sec. 4.

The absorption cross-section,  $\sigma$ , is a quantity which links the probability of absorption, expressed in area per molecule, to the quantum mechanical properties of the target molecule. The absorption cross-section is dependent on wavelength, pressure and temperature according to Eq. (5).

$$\sigma(\lambda, T, p) = \sum_{if} S_{if} \cdot g(\lambda - \lambda_{if}, T, p) \cdot n_i(T) \quad (5)$$

where  $i$  corresponds to the initial energy state and  $f$  to the final one.  $S_{if}$  is the linestrength, which corresponds to the strength of the electromagnetic transition between the initial and final energy state. The second term is the line broadening which in our case corresponds to Voigt broadening

which is a mixture of Doppler and Lorentz broadening. The last term corresponds to the populations on the various energy levels, which are given by the Boltzmann population function.

$$n_i(T) = \frac{n_0 \cdot g_i}{Z(T)} \cdot \exp(-E_i/(k_B \cdot T)) \quad (6)$$

$$Z(T) = \sum_i g_i \cdot \exp(-E_i/(k_B \cdot T)) \quad (7)$$

where  $n_0$  is the total number density of the molecules,  $g_i$  is the degeneracy at the energy level  $E_i$ ,  $Z(T)$  is the total partition function and  $k_B$  the Boltzmann constant.

In infrared spectroscopy it is possible to calculate absorption cross-sections directly from Eqs. (5) to (7) since line parameters are available for many species.<sup>25</sup> In the u.v./visible the absorption spectra are more complex and the line strengths are usually not accessible. The main temperature dependence of the absorption spectra is caused by Eq. (6), i.e., the Boltzmann population function, but there is also a temperature dependence in the line broadening, since the Doppler broadening is proportional to the square root of the temperature, and the Lorentz broadening is inversely proportional to the temperature.

NO exhibits several absorption bands in the far u.v.<sup>26</sup> of which the absorption region 196–228 nm is suitable for DOAS measurements. Calculations of the absorption spectra of NO for the  $\gamma(0,0)$  band around 226 nm, were therefore carried out at various temperatures and column densities using a PC-based computer code which was developed from algorithms by Wahnström.<sup>27</sup> Molecular parameters from Huber and Herzberg<sup>26</sup> were used to calculate energy levels and transition strengths. The  $\gamma(0,0)$  band corresponds to an electronic transition from the ground state  $X^2\Pi$  to the upper level  $A^2\Sigma$  on which a vibrational transition and many rotational transitions are superimposed. At the ground state the behavior of NO was approximated to that of a Hund's case (a) molecule,<sup>28</sup> meaning that the spin-orbit interaction is stronger than the orbit-rotation interaction, which is a good approximation for low rotational quantum numbers. Due to increasing population at higher rotational levels with increasing temperature, the latter assumption is better at lower than at higher temperatures. At the upper level,  $A^2\Sigma$ , on the other hand, NO behaves like a Hund's case (b) molecule, since this is always the case for all  $\Sigma$  states.

The temperature was introduced through the Boltzmann population function by which the transition strengths were multiplied, considering both rotational and vibrational Boltzmann distributions. Neither the oscillator strength, nor the Franck-Condon factor were calculated. Instead the Hönl-London transition strengths were calculated as relative values using algorithms derived by Hill<sup>29</sup> and included in the program by Wahnström.<sup>27</sup> In order to obtain absolute absorption cross-sections the calculated spectra were compared with and scaled to experimental spectra. The calculated absorption cross-sections at various temperatures were then converted to DOAS spectra at atmospheric pressure. This was performed by adding Voigt broadening, with a pressure broadening coefficient of  $0.56 \text{ cm}^{-1}$ , to the calculated absorption cross-sections.<sup>30</sup> The absorption cross-sections were then convoluted with the *instrument line shape* (ILS) function for the DOAS instrument in use, yielding atmospheric DOAS spectra. The ILS function was obtained by recording the line profile of a low-pressure mercury lamp at 253.8 nm with the DOAS instrument, and then compensating for a slightly lower spectrometer dispersion at 226 nm.

#### 4. RESULTS

The change in the spectral features with changing temperature between 20 and 450°C was studied. The main reason for the temperature effect in this temperature region is redistribution of the population on the rotational levels, which means that certain absorption lines will gain in absorption strength at the expense of others, according to the Boltzmann population function, as was described in Sec. 3. In order to get a feeling for the possible potential effects it can be mentioned that for a change in the temperature of 400 K the rotational energy level with the maximum population will move 3.5 meV, which corresponds to 1–5 nm in wavelength units in the u.v./visible region. What is interesting from the DOAS point of view is how the redistribution of the population

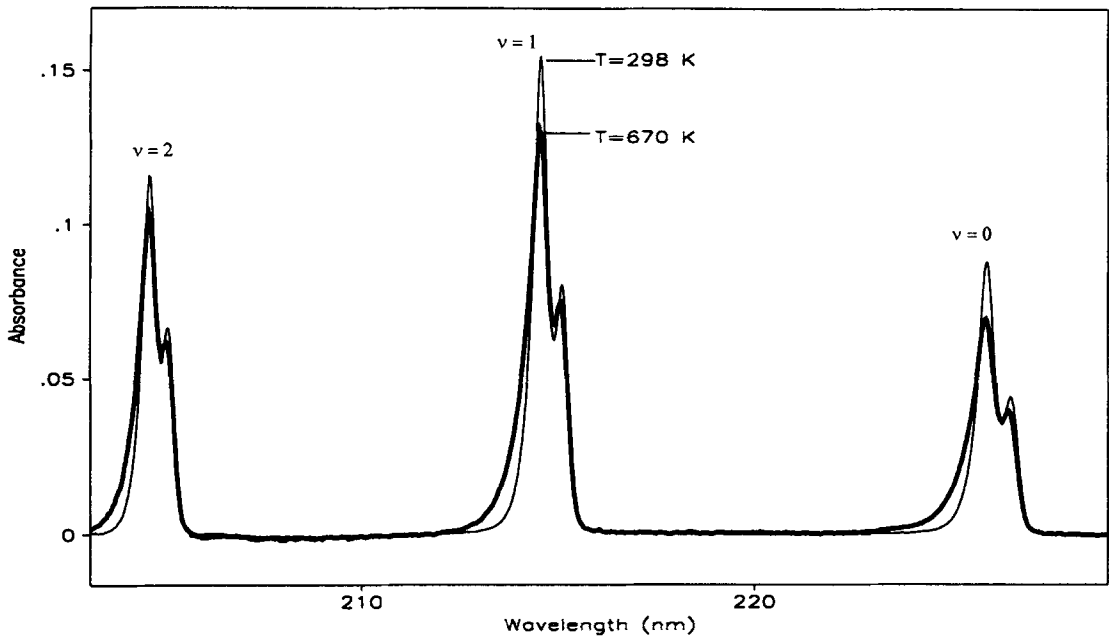


Fig. 4. Experimental absorbance spectra of NO at two temperatures, 298 and 670 K, at the  $\gamma(0,0)$ ,  $\gamma(0,1)$  and  $\gamma(0,2)$  bands.

of the rotational levels affects the differential absorption features, and what kind of errors this can cause in the retrieved total columns.

#### 4.1. Nitric oxide

Several transitions in the  $\gamma$  band of NO are shown in Fig. 4 at 298 and 670 K, corresponding to a total column of  $54.9 \text{ mg/m}^2$ . It can be seen that an increase in the temperature leads to a lowering of the absorption peaks in favor of the surrounding structure, which for the whole spectrum leads to a smoothing of the absorption structure. In contrast to the other species in this study, NO does not exhibit any broad absorption features. This makes it possible to derive a baseline spectrum by fitting a spline through the background and the whole absorption structure can therefore be used for measurements. In Fig. 5 true simulated atmospheric absorption cross-sections of NO are shown for the  $\gamma(0,0)$  band around 226 nm at two temperatures, 300 and 700 K. It can be seen that the magnitudes of the absorption cross-sections decrease at the band heads with increasing temperature, in favor of other transitions with higher rotational numbers, as expected from the Boltzmann function.

In Fig. 6 results are shown from an experiment where the total columns in recorded DOAS spectra at various temperatures were evaluated, according to the procedure described in Sec. 2.4, by using a room-temperature spectrum at 300 K as the calibration spectrum. The difference in the total columns obtained by the DOAS and what was predicted by the ideal gas was interpreted as a change in the magnitude of the apparent differential absorption cross-sections caused by the temperature. The relative change in the cross-sections at a certain temperature,  $T$ , is denoted as the scaling factor,  $F(T)$ , which is plotted in Fig. 6. The same procedure was also performed for simulated spectra, obtained according to the procedure in Sec. 3, and the corresponding scaling factors are also shown in Fig. 6.

The experimental spectra were recorded at a constant volume mixing ratio (VMR) of 97 ppm, over a path length of 46 cm, corresponding to a total column of  $54.9 \text{ mg/m}^2$  at 293 K, but only to  $23 \text{ mg/m}^2$  at 700 K. It was later discovered that the NO absorption behaves linearly (obeys the Beer-Lambert law) only in a small total column range, up to approximately  $6 \text{ mg/m}^2$ , and the experimental temperature dependence measurements were thus performed in the nonlinear absorbance range for NO. The nonlinearity effect is described in Paper II.<sup>21</sup> Since the total columns in the experimental measurements varied with the temperature (ideal gas law), there is an error in

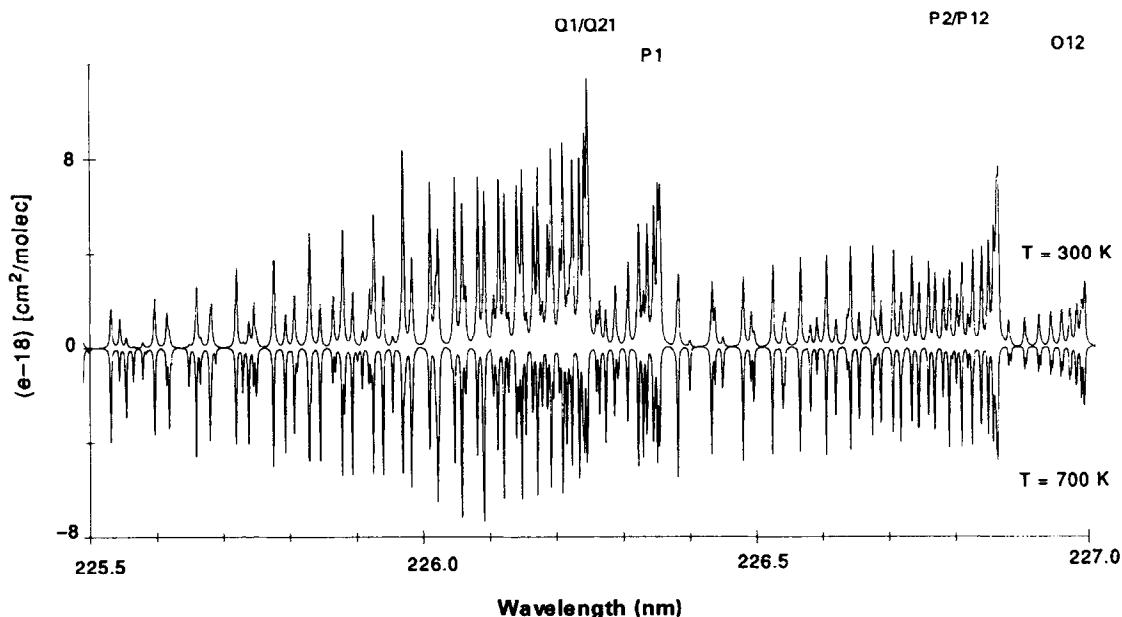


Fig. 5. Simulated Voigt-broadened absorption cross-sections of NO at 300 and 700 K and 1 atm. The sign for the cross-sections at 700 K is inverted.

the obtained experimental scaling factors in Fig. 6 due to the nonlinearity effect. In order to investigate these errors, spectral simulations, as described in Sec. 3, were performed both in the nonlinear region for a constant VMR of 97 ppm over a pathlength of 46 cm, as well as in the linear absorption region for a total column of  $6 \text{ mg/m}^2$ . As can be seen in Fig. 6 there is a rather large difference between the two types of simulations.

It can also be seen that the scaling factors for the simulation and the experiment (for the 97 ppm case) disagree by a maximum value of 5% at 700 K. The reason for this is unclear but potential error sources are: (A) it is incorrect to assume that Hund's case (a) can be used at high temperatures;

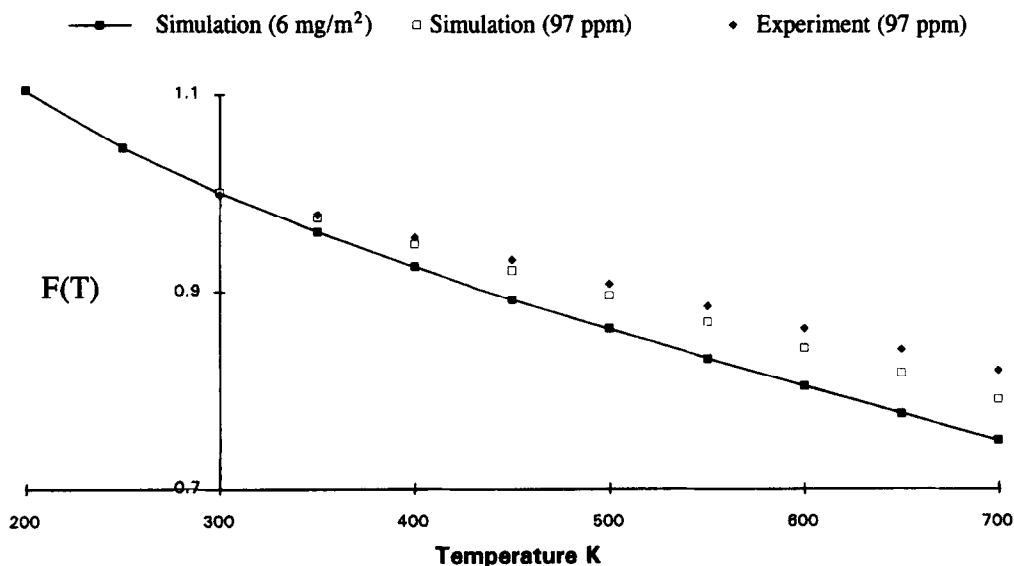
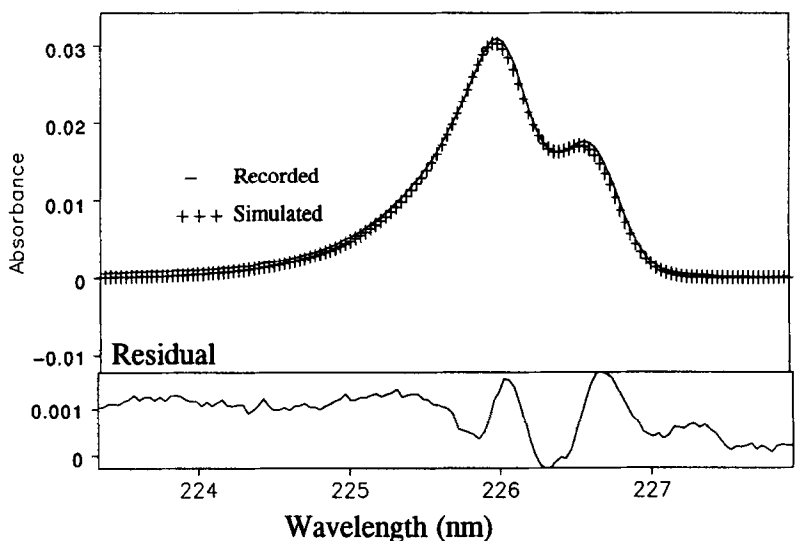
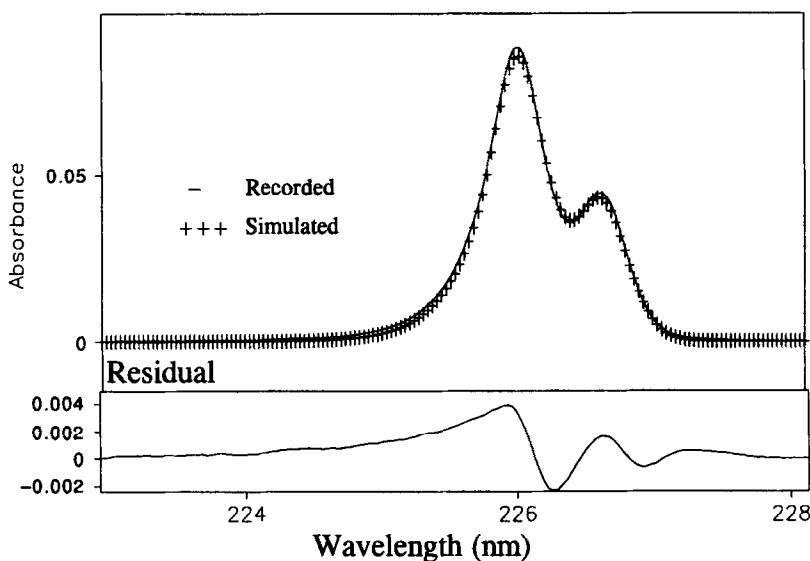


Fig. 6. Change in the relative magnitude of DOAS spectra of NO as a function of temperature. Results obtained from experimental spectra at a constant VMR (97 ppm) are displayed together with simulated spectra calculated both for a constant VMR (97 ppm) and a constant total column ( $6 \text{ mg/m}^2$ ). The optical pathlength was 46 cm.



T = 670 K



T = 300 K

Fig. 7. Experimental and simulated spectra of NO corresponding to 97 ppm over a pathlength of 46 cm for the temperatures 670 and 300 K. The residuals between the experimental and simulated spectra are also shown for the two temperature cases.

(b) the errors were caused by experimental factors, such as a reduction of the present  $\text{NO}_2$  in the calibration gas to NO at high temperatures.

The disagreement between the experimental and simulated scaling factors, in the 97 ppm case in Fig. 6, seems to be quantitative rather than qualitative, since when fitting the experimental and simulated spectra they match very well, with a correlation coefficient of 0.9995 both at room temperature and at the higher temperature. This can be seen in Fig. 7 where the simulated and experimental spectra are displayed together with their residue spectra.

In Fig. 8 the effect of spectral resolution on the scaling factor is illustrated by a comparison of simulations performed at 1 and 0.3 nm resolution. It can be seen that the scaling factor is considerably more temperature sensitive for the higher spectral resolution than for the lower one. This can be understood by the fact that with the lower spectral resolution the apparent redistribution of the rotational population will be less pronounced, since the band-pass of the

instrument will, to a larger extent, cover both the lines which gain and lose absorption strength. It can thus be concluded that the higher the spectral resolution the larger the apparent temperature sensitivity of the spectra.

#### 4.2. Sulfur dioxide

DOAS measurements of  $\text{SO}_2$  can be performed in two spectral regions in the u.v.: 260–340 and 200–230 nm. The spectral features are very complex and poorly understood in the 260–340 nm region due to the fact that two upper electronic levels are coupled,  ${}^1A_2$  and  ${}^1B_1$ . Analyses of the rotational structure have shown that most of the absorption bands and most of the discrete structure correspond to the electronic transition ( ${}^1A_2 \leftarrow {}^1A_1$ ), although this transition is actually forbidden.<sup>31–33</sup> The ( ${}^1A_2 \leftarrow {}^1A_1$ ) transition becomes allowed by vibronic coupling between the electronic levels  ${}^1B_1$  and  ${}^1A_2$ . The underlying continuum in the absorption spectrum is explained by the transition ( ${}^1B_1 \leftarrow {}^1A_1$ ). Only a few studies regarding temperature effects on the absorption cross-sections of  $\text{SO}_2$  have been performed. Brown<sup>34</sup> conducted a study in which absorption spectra of  $\text{SO}_2$  around 300 nm were collected on photographic plates, at temperatures between 20 and 1000°C. Woods<sup>35</sup> recorded high-resolution absorption cross-sections (0.002 nm) of  $\text{SO}_2$  at 293 and 373 K, using a dye laser between 297 and 301 nm, while McGee<sup>36</sup> made recordings of the absorption cross-sections of  $\text{SO}_2$  at 295 and 210 K, for wavelengths between 300 and 324 nm. The  $\text{SO}_2$  absorption between 200 and 230 nm corresponds to the electronic transition ( ${}^1B_2 \leftarrow {}^1A_1$ ). In this region predissociation occurs below 219 nm.<sup>32</sup> This results in diffuse absorption features below 196 nm.<sup>36</sup> No studies were found in the literature in which the influence of temperature above 20°C was reported for  $\text{SO}_2$  between 200 and 230 nm. There are, however, a few studies in which the absorption cross-sections were recorded at temperatures below room temperature.<sup>37,38</sup>

4.2.1.  $\text{SO}_2$  around 300 nm. In Fig. 9 (a) absorbance spectra of  $\text{SO}_2$  are displayed around 300 nm. They were recorded at a total column of 236 mg/m<sup>2</sup> at two temperatures: 298 and 671 K. The peaks were labeled according to the convention of Clements.<sup>39</sup> It can be seen that the absorbance peaks decrease with increasing temperature while the valleys in the spectra increase; the band integral of the absorbance versus wavelength seems to be constant, however. Increasing temperature thus leads to a smoothing of the spectral features. This is consistent with the findings of Woods,<sup>35</sup> where the absorption peak at 300.06 nm decreased by a factor of 0.79 and the absorption minima around 299.3 nm increased with a factor 1.17, when increasing the temperature from 293 to 373 K. The results also agree qualitatively with those of Brown<sup>34</sup> where a smoothing of the photographic traces of  $\text{SO}_2$  was seen when increasing the temperature from 293 to 1273 K. In Fig. 9 (b) the differential

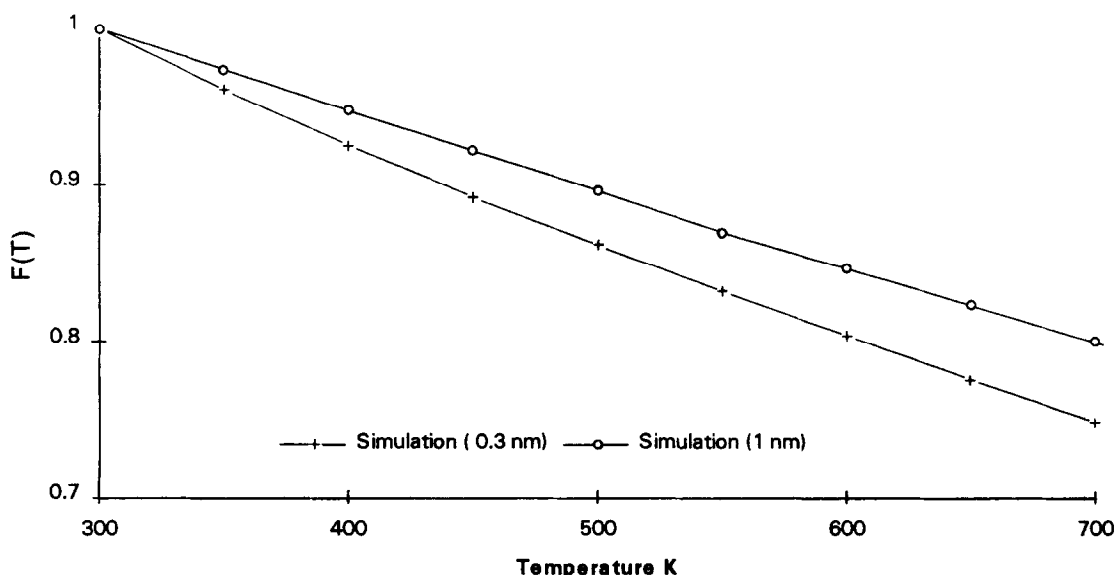


Fig. 8. Dependence of resolution on the temperature effects simulated for NO for a total column of 12.6 mg/m<sup>2</sup> at 0.3 and 1 nm resolution.

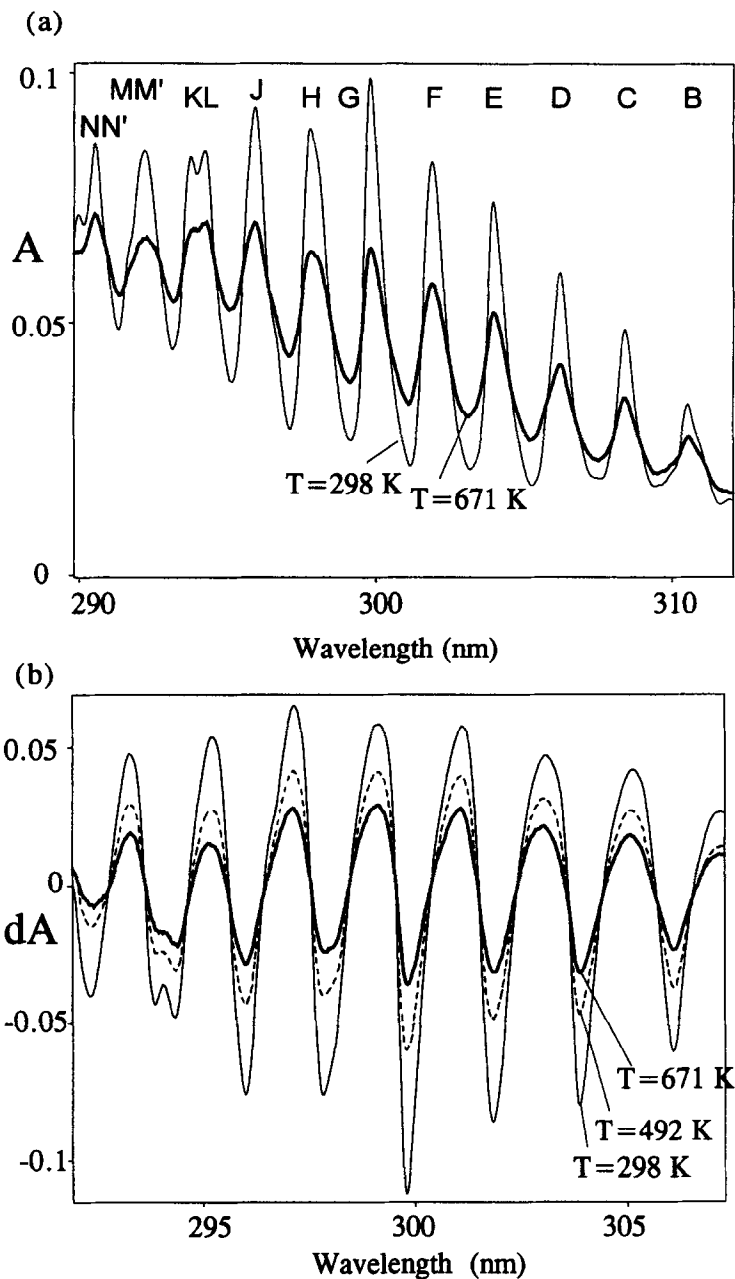


Fig. 9. (a) Absorbance spectra of  $\text{SO}_2$  at 300 nm recorded at 298 K (fine) and 671 K (broad) and corresponding to a total column of  $236 \text{ mg/m}^2$ ; (b) differential absorbance spectra (3rd order) at several temperatures corresponding to the spectra in (a).

absorbance spectra that correspond to the absorbance spectra are also shown. These were evaluated according to the DOAS algorithms that were described above. The initially recorded spectra were then normalized with a lamp spectrum, and fitted and divided with a third order polynomial. It is worth mentioning that the absorbance is defined with the decimal logarithm while we define the differential absorbance with the natural logarithm and with the opposite sign convention, according to Eq. (4).

4.2.2.  $\text{SO}_2$  between 210 and 230 nm. In Fig. 10 absorbance spectra of  $\text{SO}_2$  in the spectral region 210–230 nm are shown, recorded at 298 and 614 K and corresponding to a total column of  $236 \text{ mg/m}^2$ . The peaks were labeled according to the convention of Okabe.<sup>40</sup> It should be noted how the peak absorption strength increases towards the red side of the spectrum while it decreases

towards the blue side with increasing temperature, with band No. 6 at 222 nm as a turning point. At the same time, the absorbance in the regions of the valleys increase with increasing temperature over the whole region shown. This behavior is in good qualitative agreement with Martinez,<sup>38</sup> in which the absorption spectra of SO<sub>2</sub> between 210 and 230 nm were recorded at room temperature, at 0.1 nm resolution, and then compared with other recordings at 213 K performed by Freeman.<sup>37</sup>

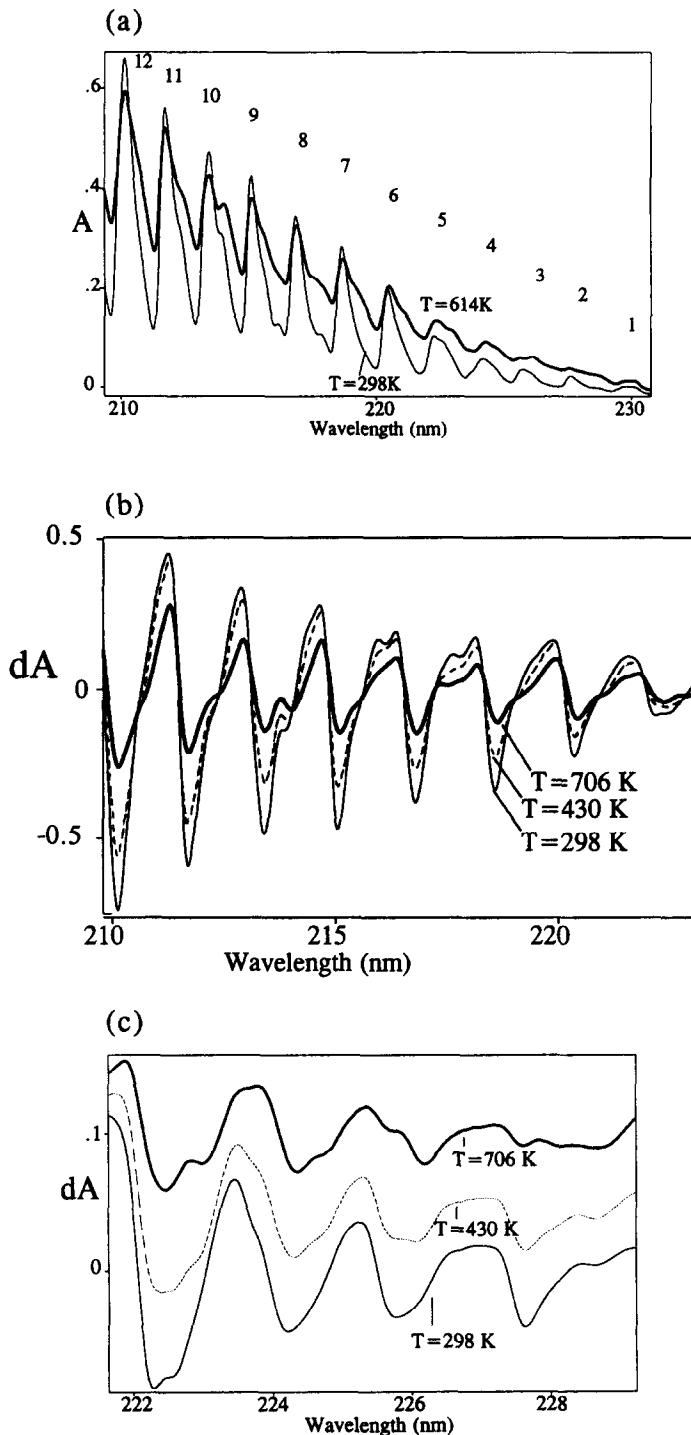


Fig. 10. (a) Absorbance spectra of SO<sub>2</sub> at 298 and 614 K at a total column of 236 mg/m<sup>2</sup>, (b) differential absorbance spectra (5th order polynomial) between 210 and 222 nm corresponding to the spectra in (a); (c) differential absorbance spectra (5th order polynomial) of SO<sub>2</sub> between 222 and 228 nm.

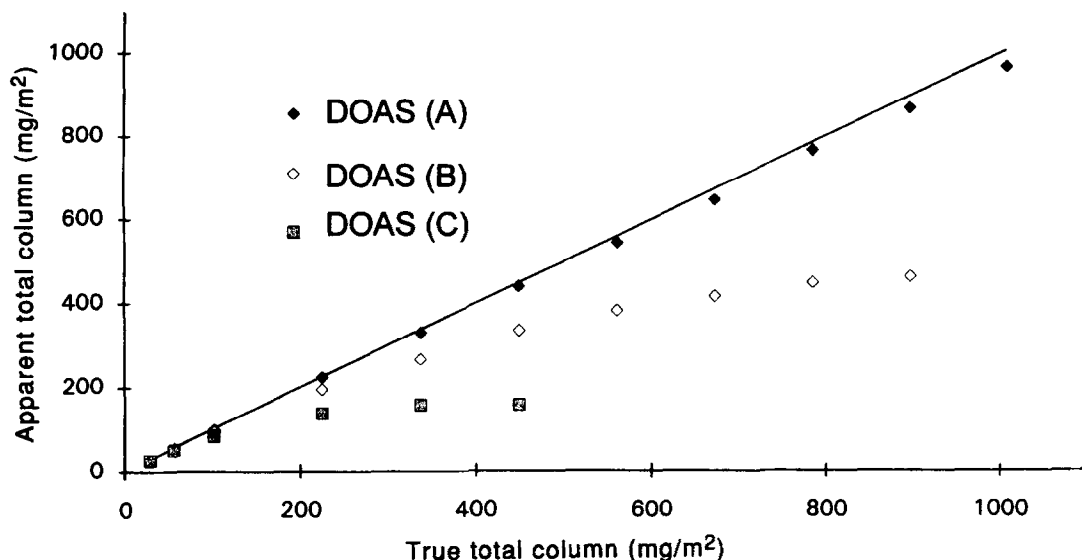


Fig. 11. Apparent total column of  $\text{SO}_2$  evaluated by DOAS as a function of true total column at 300 K. Evaluation regions (A): 223–228 nm, (B): 216–220 and (C): 208–211 nm.

The increasing absorption strength above 222 nm with increasing temperature was explained by increasing hot band transitions, a phenomenon which was also observed for the absorption of ammonia in this study. The corresponding differential absorbancies of  $\text{SO}_2$  (5th order polynomial) are also shown in Fig. 10.

Since the magnitudes of the absorption cross-sections for  $\text{SO}_2$  change rapidly in the spectral region displayed in Fig. 10, the absorbance can behave linearly in one region of the spectrum while behaving nonlinearly in another region. Several plots of apparent total column as a function of true total column are displayed in Fig. 11, where the apparent total columns were evaluated using the room temperature differential absorption cross-sections in Fig. 10 and by using different evaluation intervals. The apparent differential absorbance behaved linearly to approximately  $90 \text{ mg/m}^2$  for the evaluation interval 223–228 nm (region A), while it was linear only to  $6 \text{ mg/m}^2$  when the left part of the spectrum, 208–211 nm (region C), was being used. This type of deviation from the Beer–Lambert law, so-called nonlinearity effects, have been studied extensively in Paper II.<sup>21</sup>

In Paper II<sup>21</sup> it will be shown that the main effect of the nonlinearity is a reduction in the apparent peak height. The spectra in Fig. 10 were recorded at a constant VMR of 196 ppm over a pathlength of 46 cm, and this corresponds to a total column of  $236 \text{ mg/m}^2$  at room temperature, but only to  $99 \text{ mg/m}^2$  at 706 K. The peaks on the blue side in the room-temperature spectra in Fig. 10 will therefore be suppressed, in comparison with the peaks in the other spectra which were recorded at higher temperatures. The absorbance peaks of the room-temperature spectra in Fig. 10 (a) will therefore be reduced by approximately 2, 14 and 40% for the evaluation regions 223–227, 216–220 and 208–211 nm, respectively. For the spectra recorded at 706 K the absorbance peaks will be reduced by 1, 6 and 17%, for the same regions.

The upper limit for linearity is considerably lower than that found by Ahmed,<sup>32</sup> where the  $\text{SO}_2$  absorbance was found to behave linearly up to  $400 \text{ mg/m}^2$  at 207.5 nm, for a spectral resolution which was only slightly smaller than ours, 0.2 nm.

#### 4.3. Nitrogen dioxide

$\text{NO}_2$  exhibits a complicated absorption spectrum between 200 and 1000 nm and few absorption bands have been analyzed thoroughly. There are several wavelength regions where DOAS measurements can be successfully performed, e.g., 210–230, 340–380 and 420–440 nm. In this study, the two latter regions were chosen and at least two electronic transitions are believed to be responsible for the absorption in these regions,<sup>41,42</sup> ( ${}^2B_1 \leftarrow {}^2A_1$ ) and ( ${}^2B_2 \leftarrow {}^2A_1$ ). We have only been

able to find one study regarding the influence of temperature above ambient, on the absorption cross-sections of  $\text{NO}_2$ .<sup>43</sup> In the low-temperature range, however, several studies have been performed in applications regarding stratospheric measurements.<sup>43–45</sup>

When performing spectral recordings of  $\text{NO}_2$  in a heated cell there are several temperature-dependent processes which must be taken into consideration since they may induce errors, i.e., photodissociation, homogeneous and heterogeneous decomposition and conversion to  $\text{N}_2\text{O}_4$ . Photodissociation was prevented for the measurements around 430 nm by using an optical filter in front of the light source with a cut-off of 410 nm. For the measurements around 360 nm, experiments were performed to ensure that the flow rate was high enough to prevent the effect of photodissociation. Another potential problem was that homogeneous and heterogeneous decomposition of  $\text{NO}_2$  to  $\text{NO}$  is thermodynamically favored. Calculations using equilibrium constants from Amirnazmi<sup>46</sup> showed that the equilibrium is significantly displaced towards the formation of  $\text{NO}$  at temperatures above 500 K, at the typical mixing ratios that were used in this study (170 ppm  $\text{NO}_2$  and 24 ppm  $\text{NO}$ ). A stop flow experiment was therefore performed in a measurement cell where a gas of  $\text{NO}_2$  and  $\text{NO}$  at the mixing ratios above was maintained at 655 K and then illuminated with visible light ( $\lambda < 410$  nm). The  $\text{NO}_2$  concentrations in the cell, which was retrieved from the DOAS instrument, followed an exponential decay very closely, with a lifetime ( $t_{1/2}$ ) of  $3.7 \cdot 10^3$  sec, and this implies a first-order reaction. Since the residence time of the gas was much shorter than the decay rate above, 30 sec in the measurement cell and 20 sec in the preheater, thermal decomposition of the  $\text{NO}_2$  gas could be neglected. The third potential calibration problem results from the fact that a considerable fraction of the  $\text{NO}_2$  will be converted to  $\text{N}_2\text{O}_4$  at low temperatures, due to the thermodynamical equilibrium  $\text{NO}_2 \leftrightarrow \text{N}_2\text{O}_4$ . Even at 50°C it was reported by Davidson<sup>43</sup> that several percent of the  $\text{NO}_2$  was converted to  $\text{N}_2\text{O}_4$ . In this study it was possible to use smaller partial pressures of  $\text{NO}_2$  than Davidson<sup>43</sup> used, due to a longer optical path in the measurement cell. Calculations using equilibrium constants from Chao<sup>47</sup> showed that the formation of  $\text{N}_2\text{O}_4$  therefore could be neglected ( $< 0.5\%$ ) at temperatures above room temperature.

In Fig. 12 the absorbancies and the corresponding differential absorbencies (3rd order polynomial) of  $\text{NO}_2$  are shown at a total column of 171  $\text{mg}/\text{m}^2$ , at 297 and 660 K. It can be seen that the differential structure is smoothed with decreasing absorbance at the peaks and increasing absorbance at the valleys, with increasing temperature. This is in qualitative agreement with the results of Davidson<sup>43</sup> who found that the differential structure was smoothed out while the integral of the absorbance changed very little with temperature. The results are also consistent with that found in the low-temperature studies of Davidson,<sup>43</sup> Bass<sup>44</sup> and Hicks,<sup>45</sup> where the absorbance spectra at 235 K displayed a considerably larger differential structure than the room-temperature spectra.

In Fig. 13 the differential absorption spectra of  $\text{NO}_2$  (3rd order polynomial) around 360 nm, corresponding to a total column of 171  $\text{mg}/\text{m}^2$ , are displayed at three temperatures: 297, 488 and 671 K.

#### 4.4. Ammonia

$\text{NH}_3$  exhibits an absorption spectrum between 180 and 230 nm corresponding to the transition ( ${}^1A_2 \leftarrow {}^1A_1$ ), which is well suited for DOAS measurements.<sup>7,8</sup> The spectrum corresponds to a progression in the  $\nu_2$  bending mode, where the vibrational transitions are spaced<sup>48</sup> by approximately 900  $\text{cm}^{-1}$ . Predissociation occurs for the whole spectrum<sup>49</sup> according to:  $\text{NH}_3 \rightarrow \text{NH}_2(X^2B_1) + \text{H}$ . The lifetimes of the excited vibrational states have been estimated by Ziegler<sup>50</sup> to be of the order of 0.1 psec, which is about 10 times longer than the vibrational periods for the molecule but considerably shorter than the rotational periods. This will broaden the rotational lines yielding a diffuse spectrum with no rotational structure and with rovibronic linewidths between 0.2 and 0.5 nm.<sup>50</sup>

In Fig. 14 recorded absorbance spectra of  $\text{NH}_3$  and their corresponding differential absorbance spectra (4th order polynomial) are shown at a total column of 14.3  $\text{mg}/\text{m}^2$ , and at 298 and 678 K. Each vibrational peak consists of an R branch towards the blue side and overlapping P and Q branches towards the red side spaced by about 70  $\text{cm}^{-1}$ . This is clearly seen for the ( $\nu_2 < 3$ ) transitions. For the high-temperature spectrum in Fig. 14, two additional peaks are seen above 220 nm. We believe that these peaks correspond to hot-band transitions originating from the

( $\nu_2 = 1$ ) ground level. Our belief is based on calculations by Harshbarger<sup>51</sup> who showed that 14% of the observed ( $\nu_2 = 0$ ) band and 4% of the observed ( $\nu_2 = 1$ ) band are due to hot-band transitions at room temperature. The qualitative behavior of the spectra in Fig. 14 with temperature is consistent with findings by Hudson,<sup>52</sup> in which increasing absorbancies above 220 nm were found at temperatures of 150 and 300°C. They also found that the bands at 217 and 214 nm shifted to the red and became triple-headed in appearance. A comparison between low- and room-temperature spectra of  $\text{NH}_3$  by Vaida<sup>48</sup> showed that the absorbance between the vibrational bands disappeared at 25 K. Ziegler<sup>50</sup> concluded that the apparent continuum in the  $\text{NH}_3$  spectrum between the vibrational bands was simply due to Lorentzian tails of the vibronic transitions.

## 5. DISCUSSION

### 5.1. Quantitative effects of temperature on the DOAS technique

The main reasons for investigating the temperature dependence of the absorption features in this study was to determine how sensitive the total columns measured with the DOAS technique were

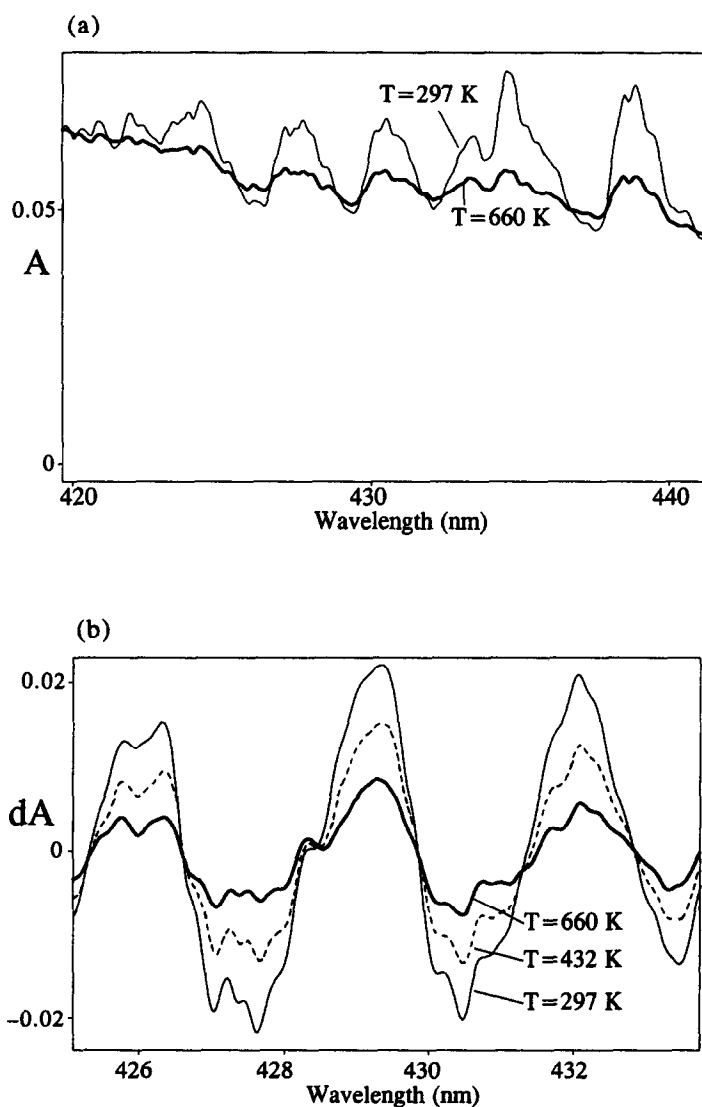


Fig. 12. (a) Absorbance spectra of  $\text{NO}_2$  at 430 nm, corresponding to a total column of  $171 \text{ mg/m}^2$  and recorded at 297 K (fine) and 660 K (broad); (b) differential absorbance spectra of  $\text{NO}_2$  (3rd order) corresponding to the spectra in (a).

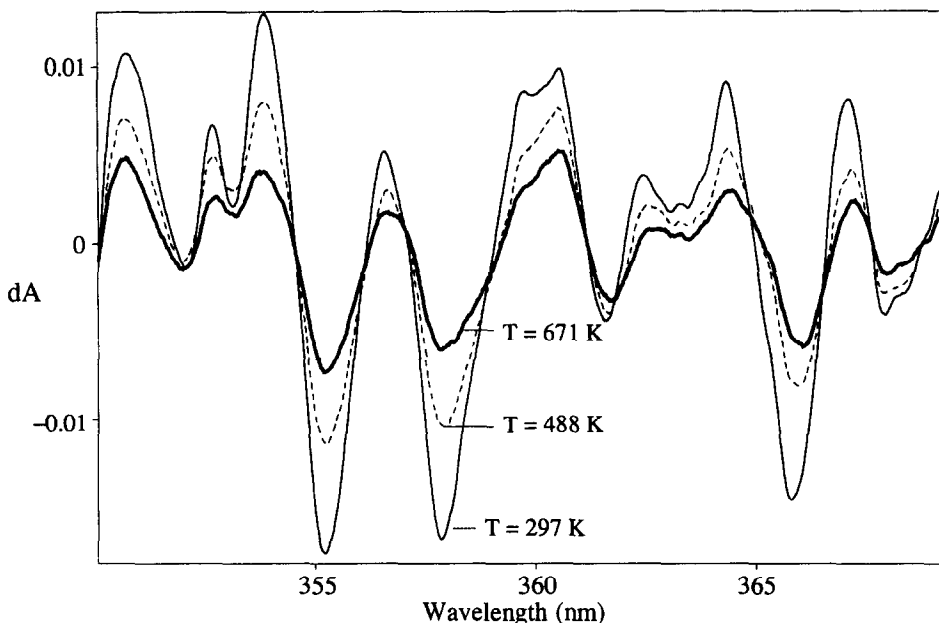


Fig. 13. Differential absorbancies of  $\text{NO}_2$  (3rd order polynomial) at 297, 488 and 671 K, for a total column of  $171 \text{ mg/m}^2$ .

to variations in the temperature. This was quantified for each species, by fitting a room-temperature differential absorption cross-section spectrum to spectra recorded at other temperatures. For each temperature a scaling factor was thus obtained corresponding to the relative change in magnitude of the differential absorption cross-section spectrum compared with the room-temperature spectrum. The temperature window studied was 290–700 K which corresponds to typical temperatures in a flue gas.

It was found, empirically, that the temperature dependence of the scaling factors could be described by the Boltzmann-like equation as given in Eq. (8). This equation was arbitrarily chosen, but reproduces the temperature behavior of the scaling factors well for many species.

$$F_{\text{temp}}(T) = K_1 - K_2 \cdot e^{-(K_3/T)} \quad (8)$$

where  $K_1$ ,  $K_2$  and  $K_3$  are variables. For the experimental data in this work a nonlinear least-square fit yielded the parameters shown in Table 1. The fitted scaling factor functions for the various species are shown in Fig. 15.

The scaling factors for NO in Fig. 15 were not obtained from experimental data but from simulated, however, since it was found afterwards that the experimental recordings of NO were performed in the nonlinear range as was previously discussed in Sec. 4. The quantitative change for all species was thus a decrease in the differential absorbance with increasing temperature, and for some of the species, i.e.,  $\text{NO}_2$  and  $\text{SO}_2$  the relative changes were of the order of 70%. The qualitative change was much less, however, and in Table 2 the change in the correlation coefficients and standard deviation in the spectral fits are shown for each species.

## 5.2. Errors

The main errors in the temperature effect study in this work can be attributed to uncertainties in the initial mixing ratios of the gases used, errors caused by potential molecular decomposition and uncertainties in temperature and pressure determinations.

An indicator of random errors can be found by comparing individual data points of measured scaling factors with the scaling factor function that was obtained when fitting Eq. (5) to the experimental data points. In Fig. 16 the relative difference between the fitted scaling factor function and measured scaling factors are shown for  $\text{SO}_2$  at 300 nm ( $\square$ ). A maximum random error of 1.5%

can be seen and this can be attributed to errors in the temperature estimation. The same type of study for  $\text{NO}_2$  showed a slightly larger discrepancy of 2.5%.

In order to estimate the systematic errors involved in the measurements a comparison of the present results with a previous study<sup>18</sup> was made. The results in the previous study were obtained from a different experimental setup with a stainless steel cell. The relative difference between the

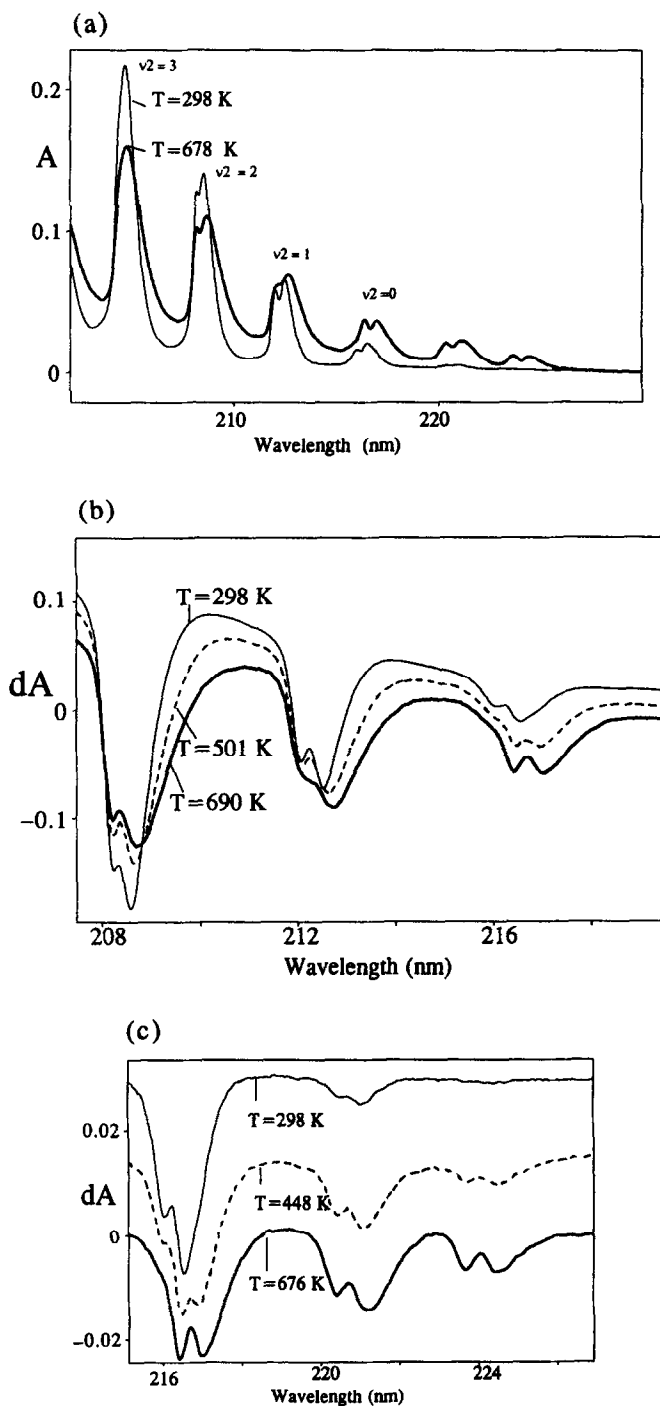


Fig. 14. (a) Absorbance spectra of  $\text{NH}_3$  at a total column of  $14.3 \text{ mg/m}^2$  at two temperatures, 298 K (fine) and 678 K (broad); (b) differential absorbance spectra of  $\text{NH}_3$  (4th order polynomial) between 208 and 218 nm corresponding to the spectra in (a); (c) differential absorbance spectra of  $\text{NH}_3$  (linear spline through end points) between 216 and 225 nm corresponding to the spectra in (a).

Table 1. Parameters for the temperature scaling factor functions. Temperature region 290 K–700 K.

Species	Spectral region (nm)	Resolution (nm)	K1	K2	K3
SO <sub>2</sub>	290–310	0.23	1.623514	2.25719	391.7548
SO <sub>2</sub>	223–228	0.30	5.6124	5.5165	52.858
NO	223–228	0.30	1.171	0.8271	483.946
NO <sub>2</sub>	425–435	0.23	2.5418	3.07873	205.84
NO <sub>2</sub>	355–365	0.23	1.41105	2.0792	484.15
NH <sub>3</sub> †	214–217	0.24	†		

†Equation (2) is not valid for NH<sub>3</sub>,  $F(T) = 1.166031 - 1.21025 \cdot 10^3 \cdot T + 3.011412 \cdot 10^{-6} \cdot T^2 - 2.701077 \cdot 10^{-7} \cdot T^3$ .

Table 2. Calculated correlations coefficients and standard deviations when fitting differential absorbance spectra at 298 K to spectra recorded at 700 K.

Molecule	Correlation coefficient	Standard deviation (%)
SO <sub>2</sub> (300 nm)	0.987	5
SO <sub>2</sub> (225 nm)	0.9095	10
NO	0.975	6
NO <sub>2</sub> (430 nm)	0.974	6
NO <sub>2</sub> (360 nm)	0.972	6
NH <sub>3</sub>	0.939	5

fitted scaling factor functions obtained from the present study and the previous one are displayed in Fig. 16 for SO<sub>2</sub> at 300 nm (◆). There is clearly a systematic difference with a maximum of 5% between the two scaling factor functions which could be caused by a larger decomposition of SO<sub>2</sub> in the stainless steel cell than in the Pyrex™ cell. The same type of discrepancy study for NO<sub>2</sub> at 430 nm yielded only a systematic difference between the different experimental setups of 0.5%. In the case of NO the potential errors are larger than for the two previous species since it was shown in Fig. 16 that there is a discrepancy of 5% between the simulations and the experimental recordings.

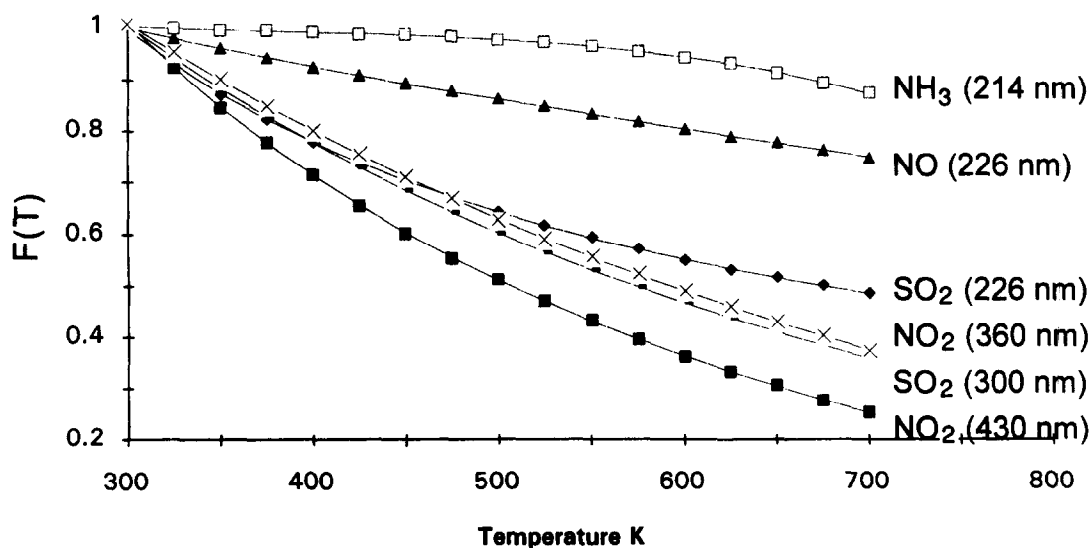


Fig. 15. Fitted functions of experimental scaling factors against temperature. The scaling factors for NO were simulated.

From the results in Fig. 16 and corresponding studies it can be concluded that both the random errors for individual scaling factor data points and the precision of the fitted scaling factor function are of the order of 2–5%, depending on molecular species. The errors in the absolute magnitude of both the differential and the absolute absorption cross-sections may be of the order of 5–10%, since some of the data were recorded from gases with a mixing precision of 3–5%, and since the errors in the temperature and pressure determination were approximated to be in the range of 1–3%. In addition to these experimental errors the choice of spectral region, polynomial, and spectral resolution may affect the quantitative results considerably, although not the qualitative results.

## 5.2. Conclusions

In this study a main problem when applying DOAS in flue gases has been investigated, i.e., temperature effects. The general effect of increasing temperature on the studied spectral features was a smoothing of the differential absorption structure with a continuous lowering of absorption peaks and raising of valleys. The overall changes in qualitative appearances of the differential absorption spectra, with the exception of  $\text{NH}_3$ , were relatively small in comparison with the large quantitative changes in magnitude. This means that deviations in temperature from the calibration spectra can cause large quantitative effects without actually being detected since the spectral fits may still be comparatively good. The two species exhibiting the largest quantitative change in differential absorption cross-section with temperature, namely  $\text{SO}_2$  and  $\text{NO}_2$  have several things in common. Both species exhibit broad-band continuous absorption spectra with differential structure superimposed on an apparent continuum caused by the presence of several electronic transitions in the wavelength regions studied. The affect of temperature was also similar and was seen as a large relative decrease in magnitude (70% decrease over 400 K) in the differential structure compared with the background, while the average over the whole absorption band actually seemed to remain almost constant.  $\text{NO}$  on the other hand, changed relatively little with temperature as did  $\text{NH}_3$  (20% decrease over 400 K). The absorption features of the latter molecule exhibited another interesting property, namely the appearance of hot-band transitions, and such a behavior was also seen for  $\text{SO}_2$  in the same wavelength region. The simulations of absorption spectra of  $\text{NO}$  indicated that the temperature effect was strongly dependent on the spectral resolution in the spectral resolution region 0.3–1 nm.

The conclusions that can be drawn from this study can be generalized to a large field of applications. The qualitative aspects of the influence of temperature on various absorption

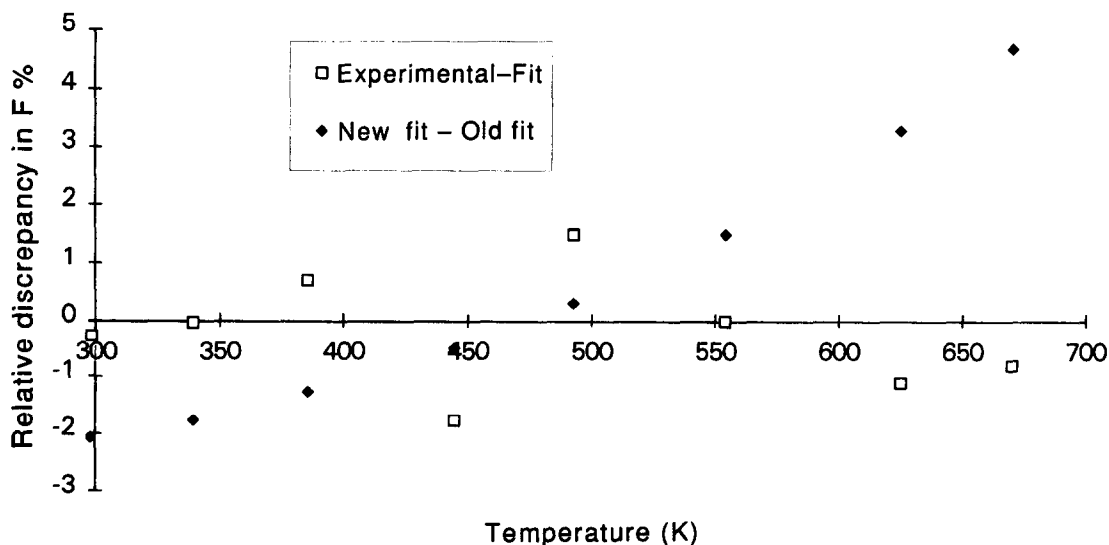


Fig. 16. (◆) Relative difference for  $\text{SO}_2$  at 300 nm between scaling factor functions obtained from recordings in a Pyrex<sup>TM</sup> and in a stainless steel. (□) Relative difference between measured scaling factor data and the fitted scaling factor function from recordings in a Pyrex<sup>TM</sup>-cell.

cross-sections are equally applicable to other dispersive measurement techniques which utilize molecular rotational transitions, for instance the technique of Fourier Transform Infrared (FTIR) spectroscopy. They are also valid in the field of atmospheric monitoring. Today, the mixing ratios of NO<sub>2</sub> and O<sub>3</sub> are being monitored in the stratosphere by the evaluation of u.v./visible differential absorption measurements from scattered sunlight. Since the differential structure of absorption cross-sections may change dramatically with temperature and since the slope of change with temperature increases with decreasing temperature it may be of importance to take the temperature effect into account, since the temperature in the stratosphere can be as low as 190 K.

*Acknowledgments*—Financial support by the Thermal Engineering Research Association, Sweden (Project B7-010/020), and by the Nordic Industrial Fund (Project 90 1669) is gratefully acknowledged.

## REFERENCES

1. G. M. B. Dobson, *Proc. Phys. Soc.* **43**, 324 (1931).
2. A. W. Brewer, C. T. McElroy, and J. B. Kerr, *Nature* **246**, 129 (1973).
3. U. Platt, D. Perner, and H. W. Pätz, *J. Geophys. Res.* **84**, 6329 (1979).
4. U. Platt and D. Perner, in *Optical and Laser Remote Sensing Techniques*, D. K. Killinger and A. Mooradian, eds., pp. 97–1059, Springer, Heidelberg (1983).
5. H. Axelsson, H. Edner, B. Galle, P. Ragnarson, and M. Rudin, *Appl. Spectrosc.* **40**, 1654 (1990).
6. H. Edner, A. Sunesson, S. Svanberg, L. Uneus, and S. Wallin, *Appl. Opt.* **25**, 403 (1986).
7. H. Edner et al, *SPIE* **1269**, 114 (1990).
8. R. Gall, D. Perner, and A. Ladstätter-Weisenmayer, *Fresenius J. Anal. Chem.* **340**, 646 (1991).
9. G. W. Harris et al, *Workshop on Optical and Laser Remote Sensing*, Monterey, CA, 8–11 Feb. D3–1 (1982).
10. H. Axelsson, H. Kloo, H. Edner, and P. Ragnarsson, *Optical Remote Sensing and Applications to Environmental and Industrial Safety Problems*, A & WMA, Houston (April 1992).
11. S. McLaren and D. Stedman, *83rd Air and Waste Management Association Annual Meeting*, Pittsburg, paper 90–86.6 (1990).
12. D. Perner and U. Platt, *Geophys. Res. Lett.* **6** (1979).
13. D. Perner et al, *Geophys. Res. Lett.* **18**, 787 (1990).
14. U. Platt and D. Perner, *Geophys. Res. Lett.* **7** (1980).
15. J. P. Pommerau and F. Goutail, *Geophys. Res. Lett.* **15**, 891 (1988).
16. S. Solomon et al, *J. Geophys. Res.* **92**, 8329 (1987).
17. A. Sarkissian, J. P. Pommerau, and F. Goutail, *Geophys. Res. Lett.* **18**, 779 (1991).
18. J. Mellqvist, H. Axelsson, and A. Rosén, *Analyst* **117**, 417 (1992).
19. J. Mellqvist, H. Axelsson, and A. Rosén, in *Inceration and Emission Control*, Berlin (June 1992).
20. A. Johansson, H. Axelsson, and J. Mellqvist, in *Optical Sensing for Environmental Monitoring*, Atlanta (October 1993).
21. J. Mellqvist and A. Rosén, *JQSRT* **56**, 209 (1996).
22. J. Mellqvist, H. Axelsson, and A. Rosén, *JQSRT* **56**, 225 (1996).
23. E. D. Hinkley, Ed., *Laser Monitoring of the Atmosphere*, Springer, Berlin (1976).
24. P. R. Bevington, *Data Reduction and Error Analysis for the Physical Sciences*, McGraw-Hill (1969).
25. L. S. Rothman et al, *JQSRT* **488**, 469 (1992).
26. K. P. Huber and G. Herzberg, *Constants of Diatomic Molecules*, van Nostrands Reinhold, New York (1979).
27. T. Wahnström, Dissertation, ISBN 91-7032-459-X, Chalmers Univ. of Technology and Univ. of Gothenburg, Gothenburg (1989).
28. F. Hund, *Zeits. Phys.* **36**, 657 (1926).
29. E. Hill and J. H. van Vleck, *Phys. Rev.* **32**, 250 (1928).
30. A. Y. Chang et al, *JQSRT* **47**, 375 (1992).
31. Y. Hamada and A. J. Merer, *Can. J. Phys.* **53** (1975).
32. S. M. Ahmed and V. Kumar, *JQSRT* **47**, 359 (1992).
33. R. Kullmer and W. Demtröder, *Chem. Phys.* **92**, 423 (1985).
34. J. Brown and G. Burns, *Can. J. Chem.* **47** (1969).
35. P. T. Woods, B. W. Jolliffe, and B. R. Marx, *Opt. Commun.* **33** (1980).
36. T. J. McGee and J. Burris Jr, *JQSRT* **37**, 165 (1987).
37. D. E. Freeman, K. Yoshino, J. R. Esmond, and W. H. Parkinson, *Planet. Space Sci.* **32**, 1125 (1984).
38. R. D. Martinez and J. A. Joens, *Geophys. Res. Lett.* **19**, 277 (1992).
39. J. H. Clements, *Phys. Rev.* **47**, 224 (1935).
40. H. Okabe, *J. Am. Chem. Soc.* **93**, 7095 (1971).
41. S. Takezava, *Chem. Phys. Lett.* **97**, 77 (1983).

42. W. Schneider, G. K. Moortgaat, and G. S. Tyndall, *J. Photochem. Photobiol. A: Chem.* **40** (1987).
43. J. A. Davidson et al, *J. Geophys. Res.* **93**, 7105 (1988).
44. A. M. Bass, *J. Res. N.B.S.* **80A**, 143 (1976).
45. E. Hicks et al, *J. Chim. Phys.* **78**, 693 (1979).
46. E. R. S. Amirnazmi et al, *J. Catal.* **30**, 35 (1973).
47. J. Chao et al, *Thermo Chim. Acta* **10**, 359 (1974).
48. V. Vaida, W. Hess, and J. L. Roebber, *J. Phys. Chem.* **88**, 3397 (1984).
49. H. Okabe, *Photo Chemistry of Small Molecules*, Wiley, New York (1978).
50. L. D. Ziegler, *J. Chem. Phys.* **82**, 664 (1985).
51. W. R. Harshbarger, *J. Chem. Phys.* **53**, 903 (1970).
52. R. D. Hudson, *Rev. Geophys. Space Phys.* **9** (1971).
53. G. Herzberg, *Molecular Spectra and Molecular Structure III, Electronic Spectra and Electronic Structure of Polyatomic Molecules*, Van Nostrand, NJ (1966).